Results in Engineering 32 (2026) 113712

Contents lists available at ScienceDirect

Results in Engineering

journal homepage: www.sciencedirect.com/journal/results-in-engineering

Research paper

Effect of Na^+ and K^+ on aluminosilicate network polymerization across alkalinity and temperature regimes: A ReaxFF reactive molecular dynamics study

Yanliang Ji [a,*], Tamino Hirsch [b], Thomas Matschei [b], Dietmar Stephan [a,*]

[a] Department of Civil Engineering, Technische Universität Berlin, Berlin, 13355, Germany
[b] Institute of Building Materials Research, RWTH Aachen University, Schinkelstraße 3, Aachen, 52062, Germany

ARTICLE INFO

Keywords:
Alkali-activated binders
Aluminosilicate clusters
Effective alkalinity
Molecular dynamics simulation

ABSTRACT

Low-calcium geopolymers derive their performance from the connectivity of sodium- and potassium-aluminosilicate hydrate networks. Here, reactive molecular dynamics simulations were used to determine how alkali type, effective alkalinity, and temperature (293 and 600 K) govern the formation and structural evolution of N-A-S-H and K-A-S-H clusters in charge-neutral, Ca-free alkaline solutions. Structures were quantified by Si and Al Qn distributions, bridging-oxygen deprotonation, T-O-T angle statistics, and the radius of gyration of the largest cluster under bond-order filtering. Lower effective alkalinity promotes polymerization in both Na and K systems, shifting Si and especially Al from Q0–Q1 toward Q2–Q4, while elevated temperature further accelerates reorganization toward higher connectivity, most clearly under lower effective alkalinity. Bridging-oxygen deprotonation increases with hydroxide availability and temperature, yielding highly charged, weakly connected aggregates at high alkalinity. In contrast, lower effective alkalinity stabilizes larger and more persistent clusters whose compositions fall within reported ranges. Together, these results show that excessive residual alkalinity leads to a less connected aluminosilicate network and that alkalinity control is important in low-calcium binders.

1. Introduction

Geopolymers are a subgroup of alkali-activated binders (AAB) and are widely regarded as a new class of low-carbon binders capable of partially replacing ordinary Portland cement in many construction applications [1–4]. They originate from the alkaline dissolution and subsequent polycondensation of aluminosilicates, yielding reaction products with high mechanical stability and excellent chemical durability [2,3]. Because of their lower carbon emissions, strong resistance to aggressive environments [5], and their ability to incorporate various industrial by-products, geopolymers have attracted considerable attention as a sustainable material for infrastructure and environmental engineering [5–7]. Further progress in geopolymer research depends on a better understanding of how aluminosilicate networks form and evolve at the molecular scale under alkaline conditions.

Low-calcium aluminosilicate precursors such as fly ash and metakaolin predominantly contain amorphous aluminosilicate phases that can be described as clusters of interconnected SiO_4 and AlO_4 tetrahedra [8–11]. Upon alkali activation, hydroxide-rich solutions initiate the dissolution of the precursor and drive the reorganization of these tetrahedral units into three-dimensional aluminosilicate frameworks [12,13]. The higher negative charge associated with AlO_4 tetrahedra is balanced by alkali cations such as Na^+ or K^+, resulting in the formation of sodium aluminosilicate hydrate (N-A-S-H) or potassium aluminosilicate hydrate (K-A-S-H) gels [10,12,14,15]. The connectivity of the evolving network, often described using Q^n notation, governs properties such as mechanical strength, ion transport resistance, and long-term stability [16–18]. Understanding how reaction conditions and alkali cations influence tetrahedral connectivity is, therefore, central to establishing structure-property relationships in low-calcium geopolymer systems.

The formation and stability of N-A-S-H and K-A-S-H clusters are governed by several interacting factors, including alkali cation type, alkalinity, solution chemistry, and temperature [12,19–21]. Alkali ions differ in ionic radius, coordination behavior, and affinity for non-bridging oxygen, while hydroxide concentration controls the dissolution and re-condensation pathways of aluminosilicate species

* Corresponding authors.
E-mail addresses: ji@tu-berlin.de (Y. Ji), stephan@tu-berlin.de (D. Stephan).

https://doi.org/10.1016/j.rineng.2026.113712
Received 3 February 2026; Received in revised form 21 September 2026; Accepted 21 October 2026
Available online 21 October 2026
2590-1230/© 2026 The Author(s). Published by Elsevier B.V. This is an open access article under the CC BY license (http://creativecommons.org/licenses/by/4.0/).
Open access funding enabled and organized by Projekt DEAL.

[20,22]. Although direct experimental characterization of these coupled processes remains challenging, extensive experimental and modeling work has been devoted to the alkali activation of slags, fly ash, metakaolin, and other nominally inert aluminosilicate precursors, where concentrated alkaline solutions dissolve Si and Al from the solid surface and promote the nucleation and growth of reaction products in the pore space [18,23–25]. For instance, bulk and spectroscopic techniques such as nuclear magnetic resonance (NMR), Fourier transform infrared spectroscopy (FTIR), and X-ray diffraction (XRD) provide essential information on average bonding environments as well as the local environments and dynamics of mobile species (e.g., alkali ions) through relaxation-based descriptors [26–28], but often lack the spatial and temporal resolution required to follow bond breaking, transient species, or rapid network rearrangements [22,29,30]. Microscale imaging methods such as Scanning Electron Microscopy (SEM) or Backscattered Electron (BSE) imaging combined with Energy-Dispersive X-ray Spectroscopy (EDX) can resolve the composition and morphology of N-A-S-H and K-A-S-H gels; however, the necessary sample preparation steps, including stopping of hydration and drying, may modify the nanoscale structure or redistribute alkalis and water, so that the measured gel compositions do not fully reflect the native hydrated state. At the structural level, the aluminosilicate network is conveniently described by the distribution of Q^n units, where Q^n denotes a tetrahedrally coordinated Si or Al sharing n bridging oxygens and assembling into chains and three-dimensional networks [31,32]. Within this framework, the specific roles of Na^+ and K^+ in altering network polymerization, as reflected in shifts in the Q^n species, under varying chemical conditions are not yet fully understood.

Molecular dynamics (MD) simulations, mesoscale kinetic modeling, and continuum approaches have been used to describe silicate dissolution, alkali-induced network disruption and dissolution–precipitation-controlled cluster growth, and to link dissolution kinetics to strength development and transport in alkali-activated binders [17,24,31,33–38]. Specifically, Sadat et al. [39] used molecular dynamics to examine how molecular water content and Si/Al ratio affect the structure and mechanical response of geopolymer binders, highlighting the strong sensitivity of Na-based clusters to hydration state and composition. Zhang et al. [40] used reactive force field molecular dynamics (ReaxFF-MD) to simulate geopolymerization of aluminate and silicate monomers into amorphous clusters. By varying the temperature (up to 1800 K) for systems with Si/Al ratios of 2 and 3, they examined how thermal history and composition affect the polymerization degree and network structure. Notably, the high-temperature protocol is a numerical strategy to enlarge clusters and access network rearrangements; it does not imply zeolite formation as in real thermal processing. Hou et al. [17] used molecular dynamics to study a N-A-S-H gel heated from 300 to 1500 K, showing water dissociation, hydroxylation of Al tetrahedra, network depolymerization, and a marked loss of stiffness with increased ductility with increasing temperature. Overall, these studies indicate that alkali hydroxides can efficiently activate nominally inert aluminosilicate particles and that Q^n-based descriptors are well suited to describe N-A-S-H and K-A-S-H clusters. However, because most simulations still focus on sodium systems or separately examine individual variables such as composition, hydration state, alkalinity, or temperature, the combined effects of alkali cation type, effective alkalinity, and thermal acceleration on the early structural evolution of Na- and K-aluminosilicate clusters remain only partly resolved.

Building on these earlier focused studies, the present work does not aim to reproduce the full precursor dissolution process but instead uses controlled Ca-free N-A-S-H and K-A-S-H cluster-forming systems to isolate how alkali type, effective alkalinity, and thermal acceleration jointly affect network polymerization and structural reorganization. The evolution of the cluster structure is quantified through Q^n distributions, bridging-oxygen deprotonation, radial distribution functions, T–O–T bond-angle statistics (T = tetrahedrally coordinated network former, i.e., Si or Al; O = bridging oxygen), cluster connectivity (R_g), and Na_2O–(K_2O)–Al_2O_3–SiO_2 ternary analysis, in order to clarify how alkali type, effective basicity, and temperature jointly influence aluminosilicate network polymerization and topology and to provide atomistic insight into composition–structure relationships relevant to low-calcium geopolymer binders.

2. Computational methods

2.1. Model construction

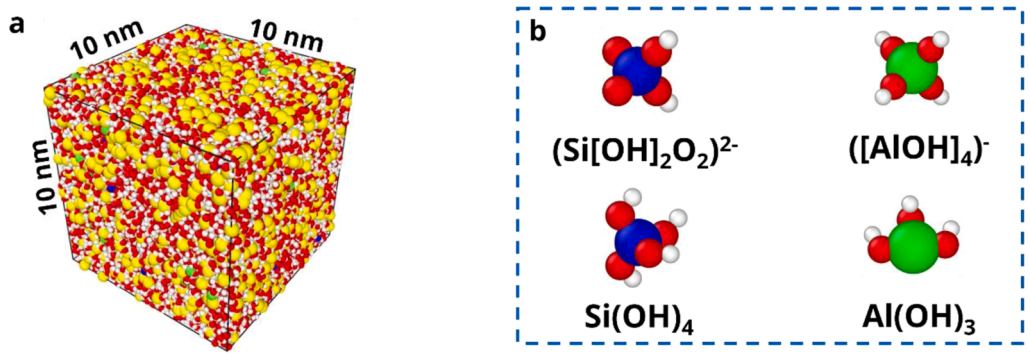
Molecular dynamics simulations were performed using the LAMMPS code with the KOKKOS acceleration framework [41–43]. The initial configurations are Ca-free, highly alkaline aluminosilicate solutions designed to investigate spontaneous cluster formation during reactive molecular dynamics simulations (Fig. 1). Each system is built as a $10 \times 10 \times 10$ nm^3 periodic cubic simulation box (Fig. 1a) and populated with representative dissolved silicate and aluminate species (Fig. 1b), explicit water, free hydroxide to control basicity, and alkali cations to provide charge compensation. The overall stoichiometry of the framework is controlled at a Si/Al ratio of 2.7, which is characteristic of low-calcium aluminosilicate gels, providing a consistent baseline network composition across the simulated solutions. The speciation includes negatively charged silicate and aluminate units that act as reactive precursors for polymerization, together with neutral hydroxide-bearing species that represent less deprotonated or non-network-forming components. Among them, SiOH represents terminal, non-bridging silanol sites, while $Al(OH)_3$ corresponds to neutral Al hydroxide species that do not initially participate in the tetrahedral aluminosilicate framework.

Boxes 1 and 2 represent the High-OH effective alkalinity condition. Both are built as $10 \times 10 \times 10$ nm^3 periodic boxes and contain a high level of free hydroxide (OH^- = 1200), establishing strongly basic conditions. The two boxes are identical in all components except for the alkali identity used for charge compensation: Box 1 contains Na^+, whereas Box 2 contains K^+, with the same total alkali content (Na^+ or K^+ = 9600). This one-variable design enables direct evaluation of the effects of Na^+ versus K^+ on the subsequent cluster formation under identical high-alkalinity conditions. This composition mimics the solution chemistry after extensive dissolution of low-calcium aluminosilicate precursors (e.g. fly ash, metakaolin) in concentrated NaOH or KOH [13,44], where Si and Al exist as molecular or oligomeric species in the pore solution and begin to repolymerize into N-A-S-H or K-A-S-H type nano-clusters.

A second set of configurations (Boxes 3 and 4) represents the Low-OH effective alkalinity condition. In these boxes, the contents of free hydroxide and alkali cations are reduced (OH^- = 100 and Na^+ or K^+ = 1600), while the number of H_2O molecules remains constant. To maintain overall charge neutrality, the initial speciation of the Si- and Al-bearing units was adjusted accordingly. Therefore, High-OH and Low-OH are treated as two effective alkalinity conditions rather than as a strict single-variable comparison of OH^- concentration. The resulting structural differences reflect the combined effects of free OH^- content, alkali availability, and charge-neutral precursor speciation. The Low-OH condition approximates a washed or neutralized geopolymer gel with reduced free OH^- and mobile alkali contents [16,45]. Simulations were performed for the four initial configurations at 293 and 600 K, resulting in eight simulation cases in total.

2.2. ReaxFF potential and computational setup

Atomic interactions were modeled using the general-purpose ReaxFF reactive force field for earth-material modeling developed by Zhang et al. [46] based on the original ReaxFF framework [47], which covers the Si–Al–O–H–Na–K system and is parameterized against an extensive DFT data set for silicates, aluminosilicates, and mineral–water systems. This force field captures coordination changes, proton transfer, and



c: Number of each species in each system

	Na^+	K^+	OH^-	H_2O	$(Si[OH]_2O_2)^{2-}$	$(Al[OH]_4)^-$	$Si(OH)_4$	$Al(OH)_3$	Silanol group
Box 1	9600	-	1200	750	3600	1200	0	300	500
Box 2	-	9600	1200	750	3600	1200	0	300	500
Box 3	1600	-	100	750	450	600	3150	900	500
Box 4	-	1600	100	750	450	600	3150	900	500

Fig. 1. Simulation box, solution species, and initial composition of the four systems. (a) Cubic MD box with periodic boundary conditions (10 nm × 10 nm × 10 nm). (b) Molecular structures of the main aqueous species used in this work: silicate $(Si[OH]_2O_2)^{2-}$, aluminate $(Al[OH]_4)^-$, monomeric silicate $Si(OH)_4$, and $Al(OH)_3$. (c) Initial absolute numbers of each species in the four simulation boxes (Box 1 to Box 4). The listed values represent species counts in each simulation box, not molar or atomic ratios.

condensation reactions over a broad range of thermodynamic conditions, making it well suited for the present simulations of hydroxylated Na- and K-aluminosilicate clusters at varying hydroxide contents and temperatures. All calculations were performed using LAMMPS [48] on the HLRN high-performance computing cluster and the Göttingen HPC facility, both of which provided the CPU-based parallel resources necessary for running large-scale reactive MD simulations efficiently [49].

2.3. Simulation protocol

Before thermal equilibration, the ReaxFF system was energy-minimized in LAMMPS using the conjugate-gradient algorithm with an energy tolerance of 1.0×10^{-4} and a force tolerance of 1.0×10^{-6} kcal mol^{-1} $Å^{-1}$. This step removed high-energy overlaps introduced during box cutting and ensured that the initial configuration entered the MD stage in a mechanically reasonable state. Equilibration proceeded in two stages. The system was first relaxed in an NPT (constant Number of particles, Pressure, and Temperature ensemble) ensemble at 100 K for 5 ps using timesteps of 0.10 fs. This low-temperature, constant-pressure time interval stabilized the density of the system while avoiding extensive chemical reactions, which are undesirable at this early stage. Once the system reached a steady volume, the ensemble was switched to NVT (constant Number of particles, Volume, and Temperature ensemble), and the temperature increased to 293 K. The system was further equilibrated for 5 ps to relax atomic positions at the target thermodynamic conditions without altering the cell volume. All production simulations were subsequently performed under the NVT ensemble at 293 K or 600 K for about 300 ps. Using NVT at this stage avoids artificial density variations caused by barostat-induced volume fluctuations, ensuring that bond formation and breaking processes arise from intrinsic chemical reactivity rather than global cell deformation. Trajectories were saved every 5000 steps, and ReaxFF bond-order information was recorded every 1000 steps for later structural analysis.

3. Results and discussion

3.1. Q^n evolution in hydroxylated systems with Na and K

Q^n distributions provide a quantitative measure of the polymerization state and medium-range connectivity of silicate and aluminosilicate tetrahedra, which is central for describing the gel backbone in N-A-S-H and K-A-S-H geopolymers. High fractions of Q^3 and Q^4 indicate more cross-linked, rigid frameworks, whereas larger amounts of Q^0 and Q^1 reflect depolymerized motifs and help distinguish the typically Si-centered N-A-S-H clusters from the often more Al-centered K-A-S-H clusters. Here, Q^n for Al is defined analogously as the number of bridging oxygen atoms around each Al atom, identified from T–O connectivity under the same ReaxFF bond-order criterion. The Al–Q^n fractions were normalized by the total number of Al atoms classified within Q^0–Q^4 (Fig. 2).

In the Na-containing systems, the Si-Q^n units exhibit a slight redistribution among Q^n species, with an increase in Si-Q^1 while Si-Q^3 and Si-Q^4 remain essentially constant. The evolution of Si-Q^n units in the K-containing systems is more stable. The variations in all Q^n species remain relatively small, suggesting that K^+ perturbs the silicate network less strongly than Na^+ and is less effective in breaking and re-forming Si-O-T linkages over the simulation time. For Al-Q^n, although some fractions are comparable between the Na- and K-containing systems, their time evolution shows distinguishable cation-dependent behavior. In the Na system, the fraction of Al-Q^0 decreases more markedly, accompanied by an increase in higher-connectivity Al-Q^n species, whereas these changes are weaker in the K system. This indicates that Al-containing units participate in network polymerization but that the Al coordination geometry remains constrained by the tendency of Al to form charge-balanced tetrahedral AlO_4 environments. Previous ^{27}Al and ^{23}Na MAS NMR results have shown that aluminum in geopolymeric gels is predominantly tetrahedrally coordinated and associated with alkali cations for charge balance, while the tetrahedral geometry of aluminum is not strongly affected by changes in Si/Al ratio or alkali cation [12]. Therefore, the observed Na-K difference in Al-Q^n is interpreted mainly as a difference in polymerization/connectivity evolution rather than a change in the fundamental Al coordination environment.

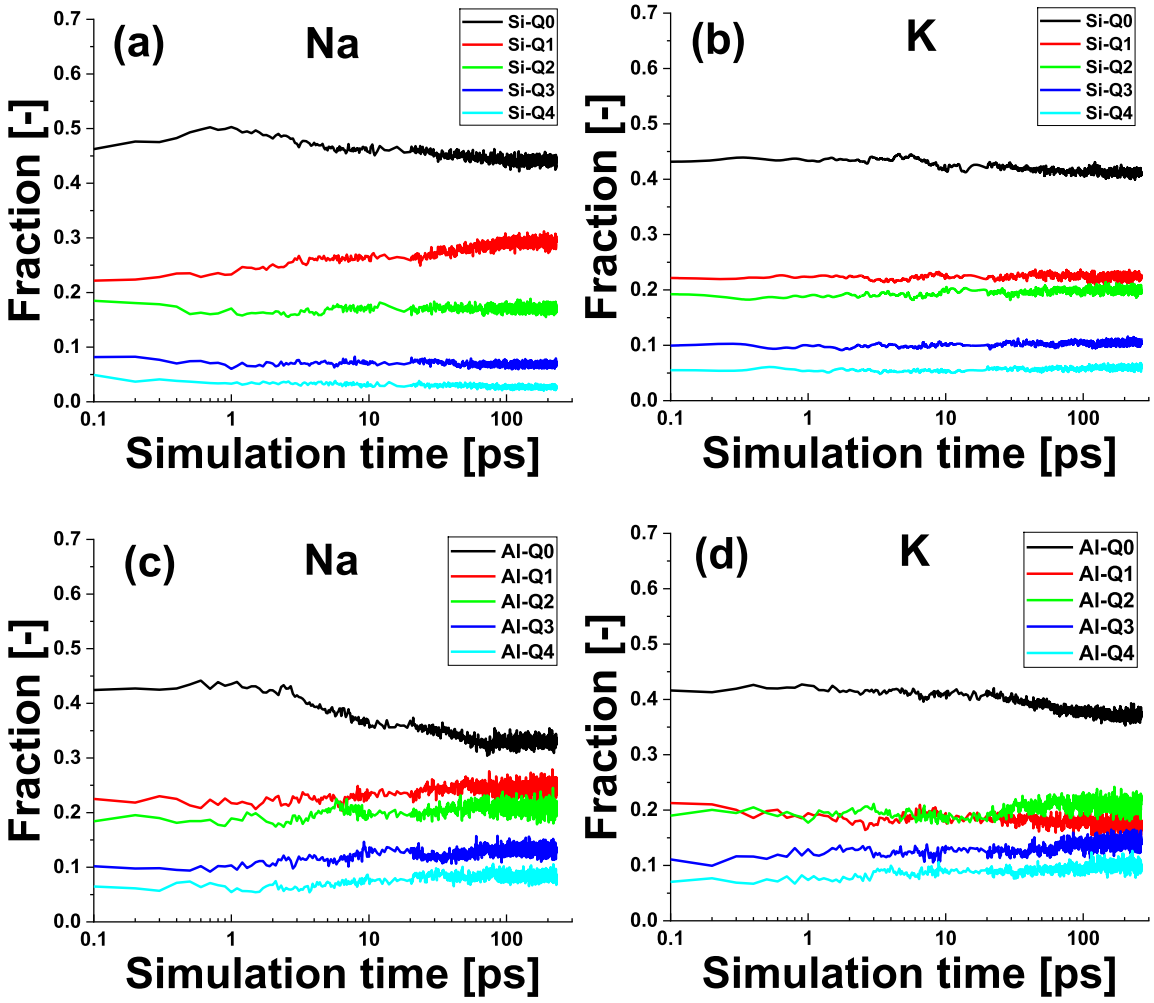


Fig. 2. Evolution of Q^n species for Si and Al tetrahedra in the presence of Na and K ions during hydroxylated simulations at 293 K (Box 1 and 2 of Fig. 1). Panels (a) and (b) show the time-dependent fractions of Si-Q^n units in the presence of Na and K, respectively. Panels (c) and (d) present the corresponding evolution of Al-Q^n species.

3.2. Q^n evolution in Na and K systems under the Low-OH effective alkalinity condition

Under the Low-OH effective alkalinity condition (see Fig. 3), the Na system shows a distinct shift in the distribution of Si–Q^n species. Si–Q^0 decreases progressively over time, while the higher-polymerized Si–Q^3 and Si–Q^4 increase. This indicates an enhanced polymerization effect promoted by Na when fewer OH groups are available to stabilize bridging oxygens.

In the K system, the evolution of Si–Q^n units is generally similar to that in the Na system. In both cases, Si–Q^3 and Si–Q^4 increase with time, indicating progressive silicate polymerization under the Low-OH effective alkalinity condition. The Al–Q^n units respond even more sensitively to the Low-OH condition. Al–Q^0 decreases markedly, accompanied by a pronounced increase in Al–Q^3 and Al–Q^4, demonstrating a strong redistribution of Al environments toward higher connectivity as polymerization proceeds. This behavior implies that Al tetrahedra become increasingly stabilized in highly connected configurations under the Low-OH condition. Overall, the Low-OH effective alkalinity condition is associated with enhanced polymerization in both the silicate and aluminate subnetworks, driving a clear shift toward higher-Q^n species over the simulated timescale.

3.3. Q^n distributions and the impact of temperature

In Fig. 4, the fractions of Si atoms in different Q^n polymerization states are shown for simulated boxes with two temperatures and two effective alkalinity conditions (High-OH and Low-OH). In both alkali systems, the silicate network is more depolymerized at High-OH at 293 K and 600 K, reflected by higher fractions of Si–Q^0 and Si–Q^1 and very low fractions of Si–Q^3 and Si–Q^4. Moving from the High-OH to the Low-OH condition results in a clear shift from low-Q^n (Q^0–Q^1) toward higher-Q^n species (Q^2–Q^4), indicating enhanced silicate polymerization. Within each effective alkalinity condition, increasing the temperature from 293 K to 600 K generally promotes polymerization, manifested by a reduced fraction of Si–Q^0 and increased fractions of higher-Q^n units, with the effect being most evident under Low-OH.

For panel (b), the K-containing system shows the same qualitative trends as panel (a). Under High-OH conditions, the distribution is dominated by low-Q^n species (mainly Si–Q^0 and Si–Q^1) with only small fractions of Si–Q^3 and Si–Q^4. Moving from the High-OH to the Low-OH condition shifts the distribution toward higher polymerization states, and increasing the temperature from 293 to 600 K further promotes Si polymerization, most clearly under Low-OH conditions. Fig. 5 shows the fraction of Al atoms in different Q^n polymerization states in simulated boxes under different alkali types, temperatures, and effective alkalinity conditions.

In both Na and K systems, the Al Q^n distributions are strongly

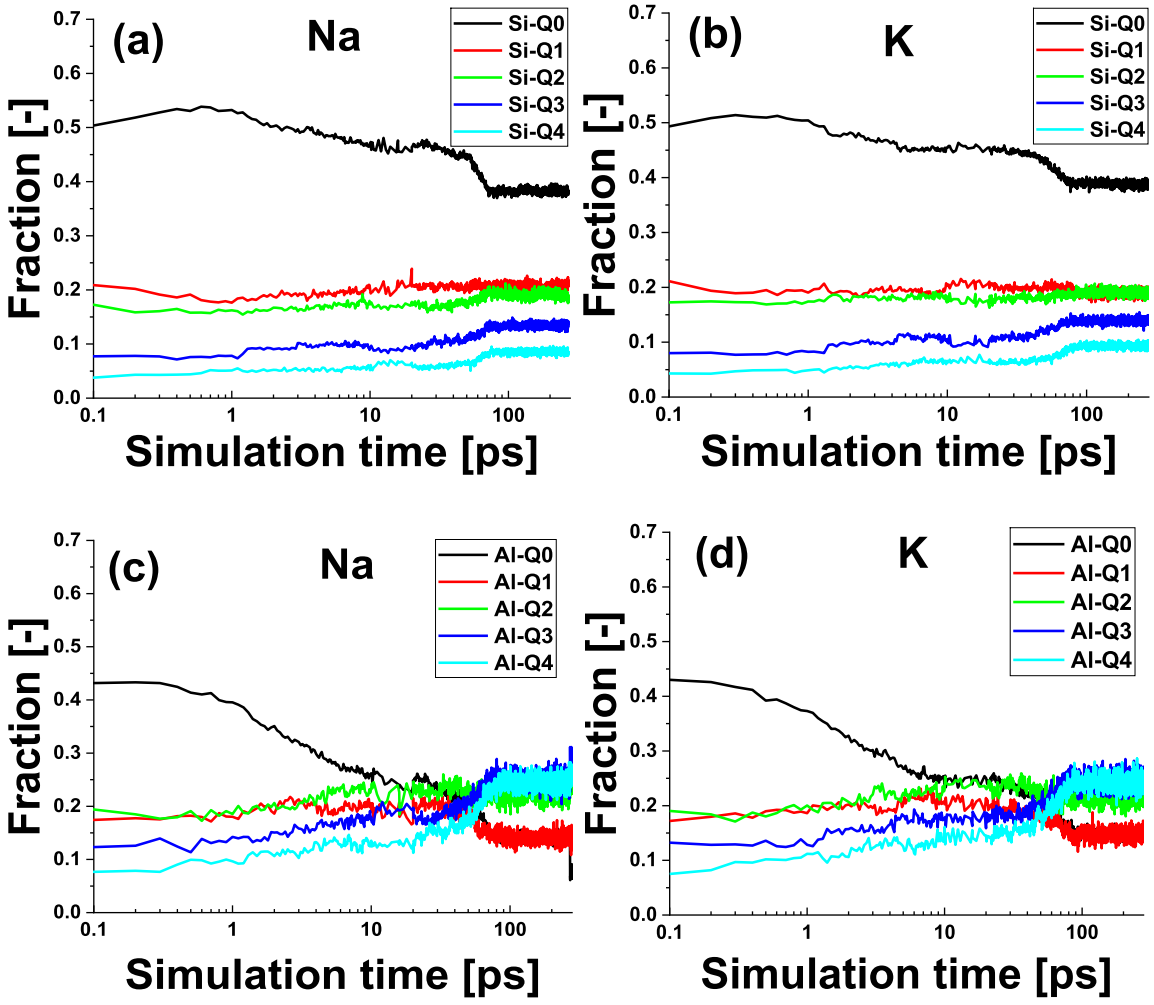


Fig. 3. Time evolution of Si–Q^n and Al–Q^n units in Na and K systems under the Low-OH effective alkalinity condition at 293 K (Box 3 and 4 of Fig. 1). Panels (a) and (b) show the changes in Si-Q^n species for Na and K, respectively, while panels (c) and (d) present the corresponding evolution of Al–Q^n units.

controlled by effective alkalinity. Under High-OH conditions at 293 K and 600 K, the Al network remains moderately polymerized, with substantial fractions of Al-Q^2 to Al-Q^4 units in addition to Al-Q^0 and Al-Q^1. When moving from the High-OH to the Low-OH condition, the distributions shift markedly toward higher polymerization states: Al-Q^3 and Al-Q^4 become the most abundant species, and Al-Q^0 is strongly suppressed, indicating that Al tetrahedra are preferentially stabilized in highly connected environments under the Low-OH effective alkalinity condition. Within each effective alkalinity condition, increasing the temperature from 293 to 600 K further promotes Al polymerization, manifested by a lower fraction of Al-Q^0 and higher fractions of Al-Q^3 and Al-Q^4, with the effect being most pronounced under Low-OH conditions.

Compared with the Si results in Fig. 4, the Al network is clearly more polymerized under all conditions. Even at High-OH, Al already shows significant fractions of Q^2–Q^4 units, whereas the Si network at the same composition is dominated by Q^0 and Q^1. Upon switching to Low-OH, the increase of highly connected Al-Q^3 and Al-Q^4 species is more pronounced than for Si, indicating a stronger tendency of Al to populate highly connected environments during polymerization. These trends suggest that Al-centered environments exhibit higher local connectivity than Si-centered environments in the simulated aluminosilicate clusters and that Al preferentially occupies the more polymerized sites, consistent with previous NMR studies on alkali aluminosilicate glasses and gels [50,51].

The 600 K simulations were used as a numerical acceleration protocol to promote bond exchange and network reorganization within the ReaxFF-MD time window, rather than to represent realistic curing or equilibrium structures above a defined glass-transition temperature. The NVT simulations reached quasi-steady pressures of approximately 0.4–0.5 GPa; therefore, possible pressure-assisted local compaction cannot be excluded. Accordingly, the 600 K results are interpreted only as comparative structural trends.

3.4. Time evolution of bridging-oxygen deprotonation

The deprotonation fraction of bridging oxygens O(BO) is used here as a simple measure of the framework protonation state under alkaline conditions: each deprotonated Si–O–T site (T = Si, Al) carries one negative charge that must be compensated by Na^+ or K^+ [52–54]. Following this fraction in time, therefore, shows how the framework charge density evolves during the MD run at different temperatures and effective alkalinity conditions. Time evolution of the deprotonation fraction of bridging oxygens O(BO) for Na systems (a) and K systems (b) at 293 and 600 K under the High-OH and Low-OH effective alkalinity conditions is shown in Fig. 6.

In Fig. 6a (Na systems), all curves show a rapid increase in the deprotonation fraction of O(BO) during the first tens of picoseconds, followed by a gradual approach to a quasi-steady plateau. The plateau level is primarily controlled by alkalinity, with the High-OH systems reaching much higher deprotonation fractions than the Low-OH systems. Within each effective alkalinity condition, increasing the temperature from 293 K to 600 K results in a systematic but smaller upward

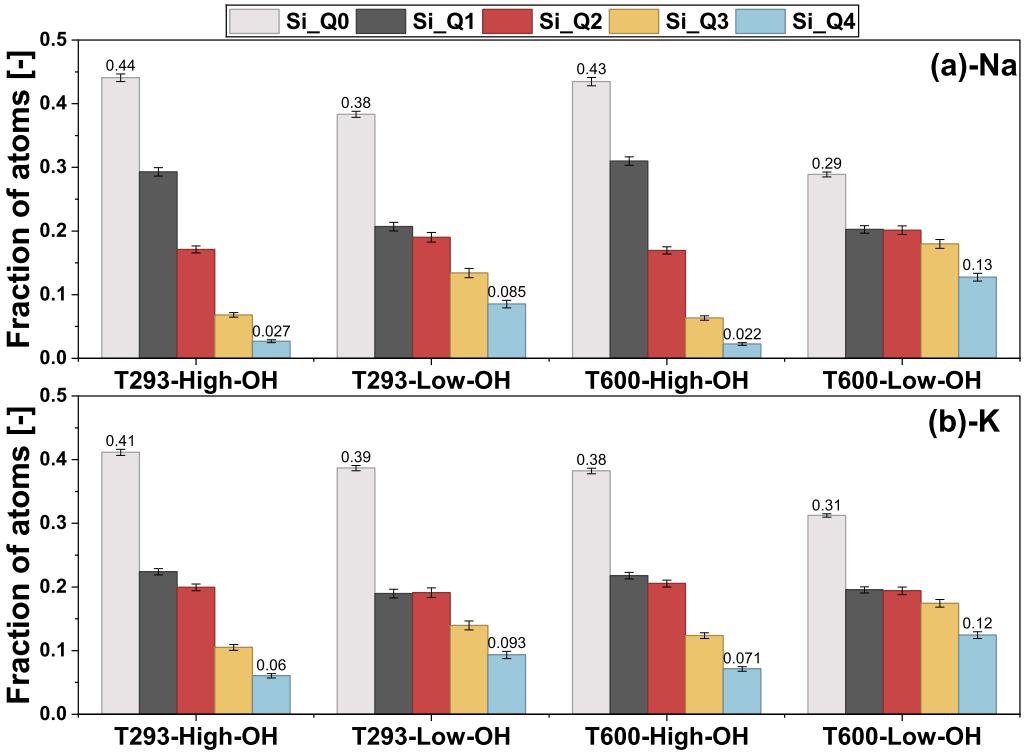


Fig. 4. Fraction of Si atoms in different Q^n polymerization states in simulated boxes under different alkali types, temperatures, and effective alkalinity conditions: (a) Na systems, (b) K systems. Error bars represent the standard deviation of the final ten saved configurations and indicate late-stage temporal fluctuations within each trajectory.

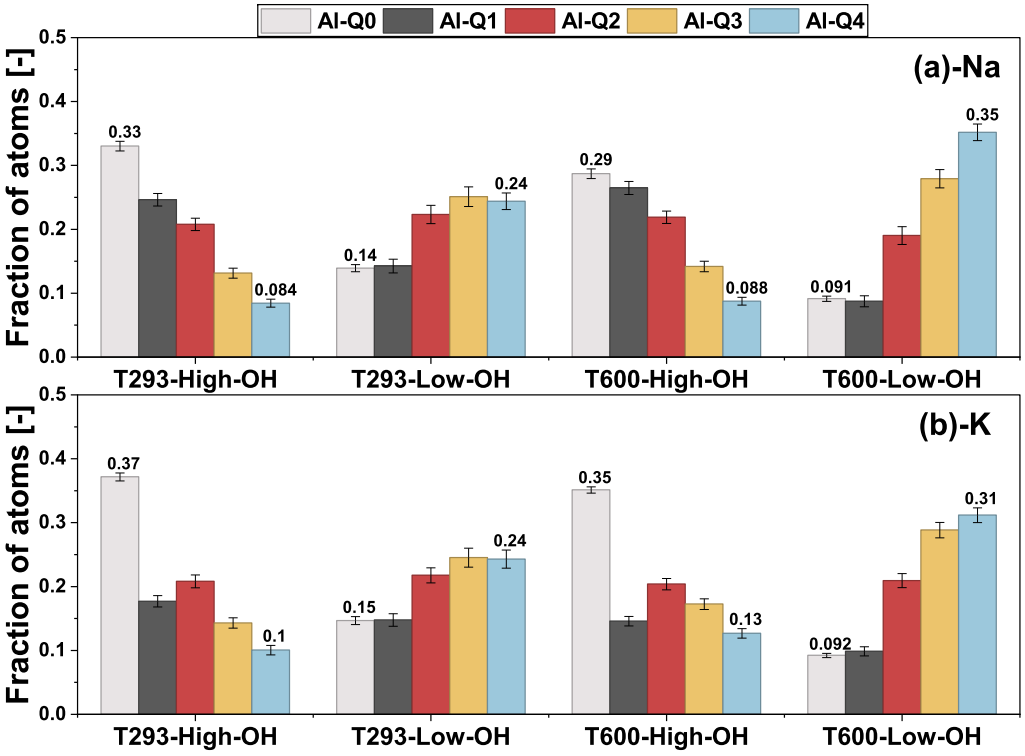


Fig. 5. Fraction of Al atoms in different Q^n polymerization states in simulated boxes under different alkali types, temperatures, and effective alkalinity conditions: (a) Na systems, (b) K systems. Error bars represent the standard deviation of the final ten saved configurations and indicate late-stage temporal fluctuations within each trajectory.

shift of the plateau, i.e., 600-High-OH > 293-High-OH and 600-Low-OH > 293-Low-OH. In Fig. 6b (K systems), the same hierarchy is observed:

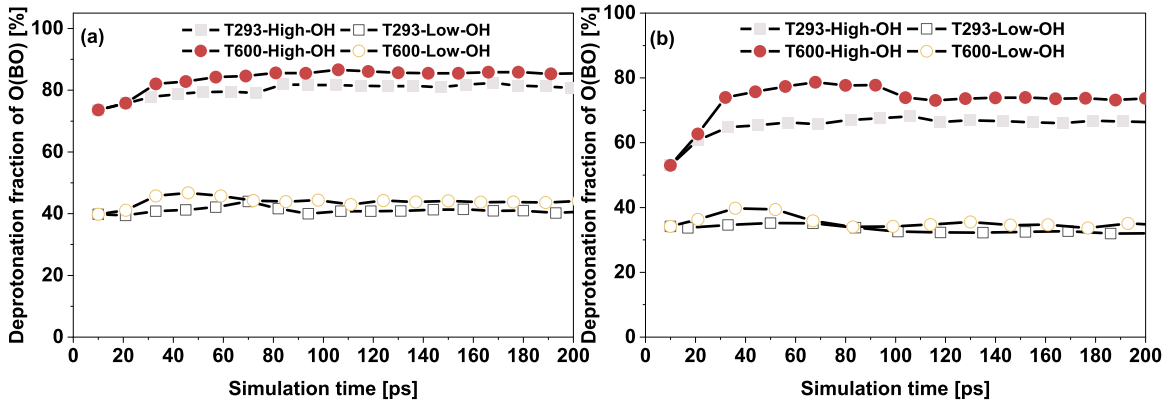


Fig. 6. Time evolution of the deprotonation fraction of bridging oxygen O(BO) for Na systems (a) and K systems (b) at 293 and 600 K under the High-OH and Low-OH effective alkalinity conditions.

High-OH produces substantially higher O(BO) deprotonation than Low-OH, and higher temperature again increases the plateau value. The curves approach their steady levels more gradually, but the overall ordering between High-OH, Low-OH, 293 K, and 600 K remains the same. This trend is consistent with interfacial spectroscopy and dissolution studies showing that increasing temperature and modifier/OH content promote proton transfer and shift the equilibrium toward more negatively charged framework oxygens [52,53]. At the same time, ion-specific effects of Na^+ and K^+ modulate the acidity of surface silanol/aluminol groups and the stability of deprotonated sites [55].

3.5. Short-range structure and coordination revealed by RDFs

The radial distribution function g(r) describes the probability of finding two atoms at separation r relative to a random distribution, thereby revealing characteristic bond lengths and local coordination environments [17,56,57]. In Fig. 7, the partial radial distribution functions g(r) for Si–O, Al–O, and alkali–O pairs (Na–O or K–O) in the High-OH, Low-OH systems at 293 K and 600 K for Na and K systems are shown. The first sharp peaks of Si–O and Al–O are located around typical tetrahedral bond distances, followed by a broader alkali–O peak at larger r, reflecting the more weakly bound, charge-compensating role of alkali cations in the network. To further quantify the alkali-O coordination environments, a normalized first-shell coordination descriptor, CN^*, was calculated by integrating $4\pi\rho_O^0 g(r)r^2$ up to the first minimum after the corresponding alkali-O RDF peak, where ρ_O^0 was evaluated from the total number of O atoms and the common initial box volume. The use of ρ_O^0 minimizes artificial differences caused by void space, amorphous

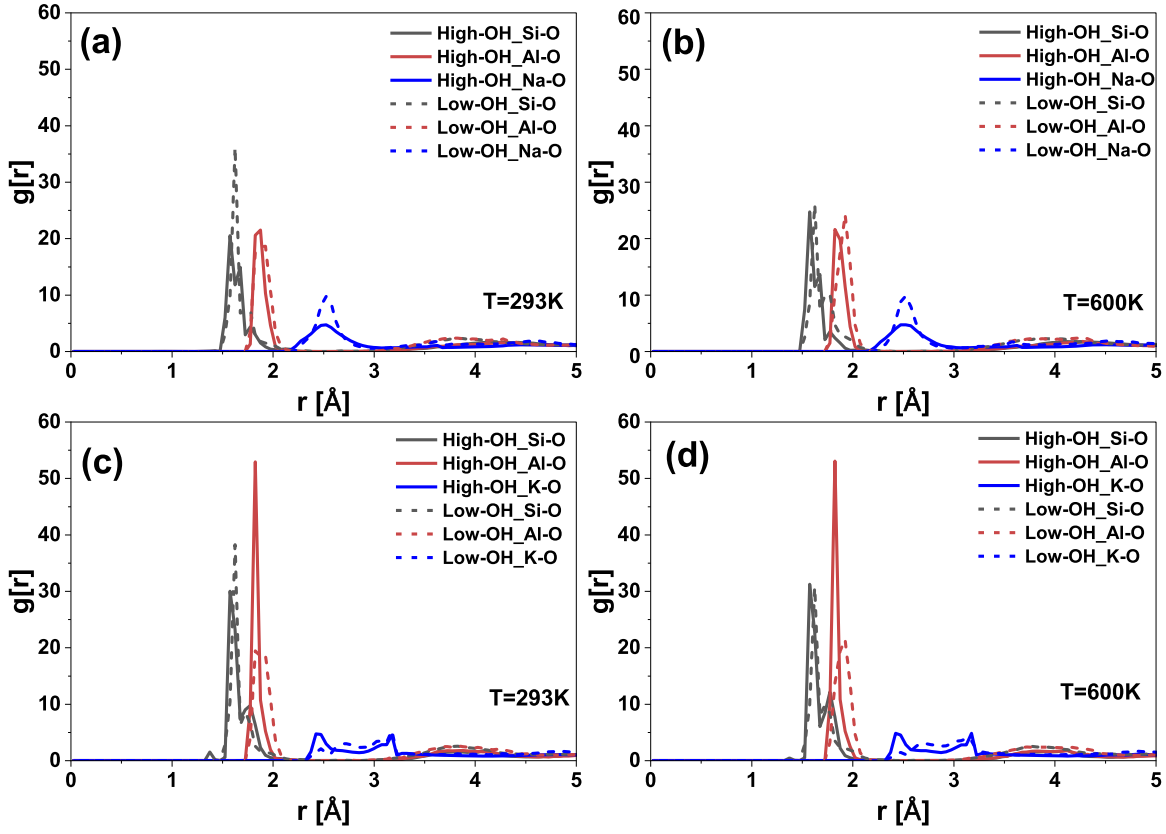


Fig. 7. Partial radial distribution functions g(r) for Si–O, Al–O, and alkali–O pairs (Na–O or K–O) in the High-OH and Low-OH conditions for the Na system at 293 K and 600 K (a, b) and for the K system at 293 K and 600 K (c, d).

cluster packing, and different NPT-relaxed box volumes. The resulting CN^* values are listed in Table 1 and are used for relative comparison rather than as absolute coordination numbers of a homogeneous gel phase.

The peak positions change only marginally between 293 and 600 K and between High-OH and Low-OH conditions, indicating that the average T–O bond lengths (T = Si, Al) are essentially preserved. In contrast, the peak heights and widths show systematic variations, most clearly for the Na–O pair. At both temperatures, the Low-OH systems display a higher and sharper first Na–O peak than the corresponding High-OH systems, consistent with a more localized Na coordination under the Low-OH condition, and the aluminosilicate network is more polymerized. The Al–O peak also becomes slightly sharper in the Low-OH systems, particularly at 600 K, reflecting a more well-defined AlO_4 tetrahedral environment under the Low-OH effective alkalinity condition. Increasing the temperature from 293 to 600 K mainly results in modest broadening and smoothing of the second-shell features, while the first-shell peaks remain largely unchanged, consistent with enhanced thermal motion without major rearrangement of the primary T–O tetrahedral framework. The normalized first-shell coordination descriptor CN^* provides a semi-quantitative support for this interpretation. For Na-O, CN^* changes only moderately, from 3.92 to 4.46 at 293 K and from 4.00 to 4.52 at 600 K when moving from High-OH to Low-OH conditions. This agrees with the sharper Na-O RDF peaks under Low-OH conditions and indicates a slightly more populated and localized Na-O first coordination shell. In contrast, the K-O CN^* values show stronger condition dependence, ranging from 4.62 to 4.74 at 293 K and from 4.63 to 6.44 at 600 K. The higher CN^* of K-O under the 600 K Low-OH condition is consistent with the broader and more diffuse first-shell coordination of K^+. Therefore, the integrated RDF analysis supports the conclusion that Na^+ forms a more localized oxygen coordination environment, whereas K^+ exhibits a more flexible and condition-sensitive coordination shell.

In the K systems, the Al–O peaks are lower for the Low-OH compositions than for the corresponding High-OH ones at both 293 and 600 K. This indicates a modest broadening of the T–O bond-length distributions when OH is reduced, reflecting a less tightly constrained local tetrahedral environment under the Low-OH effective alkalinity condition. This behavior can be rationalized by the fundamental ion properties of K^+ compared with Na^+. K^+ has a larger ionic radius, lower field strength, and weaker hydration/oxygen-binding affinity, which lead to more diffuse and flexible interactions with framework oxygens and weaker localization of alkali–oxygen coordination [58–60]. In contrast, the smaller Na^+ provides more localized charge compensation at negatively charged bridging- and non-bridging-oxygen sites. This interaction can stabilize charged oxygen configurations formed during deprotonation or transient Si–O–T cleavage and may confine subsequent bond exchange, reconnection, and the associated Q^n redistribution to the immediate Na-centered environment. As a result, changes in effective alkalinity in K-bearing systems are accommodated mainly through small adjustments in local bond environments rather than through strong perturbation of T–O–T linkages or large-scale rearrangement of the SiO_4 and AlO_4 tetrahedral network. Similar cation-specific effects of Na^+ versus K^+ on aluminosilicate network connectivity and alkali coordination have been reported in high-resolution NMR [59] and spectroscopic studies of silicate and aluminosilicate glasses and melts, as well as in hydration studies of alkali ions.

Table 1
Normalized first-shell coordination descriptors CN^* for Na-O and K-O pairs.

System	Pair	r_{min}(Å)	CN*
293 K High-OH	Na-O	3.075	3.92
293 K Low-OH	Na-O	3.025	4.46
293 K High-OH	K-O	3.225	4.62
293 K Low-OH	K-O	3.225	4.74
600 K High-OH	Na-O	3.075	4.00
600 K Low-OH	Na-O	3.025	4.52
600 K High-OH	K-O	3.225	4.63
600 K Low-OH	K-O	3.625	6.44

3.6. Bond angle distributions and network topology

T–O–T (T = Si, Al) bond angles are a key indicator of the topology and flexibility of aluminosilicate clusters, as they reflect the degree of tetrahedral rotation, ring-size distributions, and the extent of network polymerization [16,17,56,57]. Variations in these angles, therefore, provide insight into how composition and temperature influence local connectivity and structural rearrangements. Bond angle distributions for Si–O–Si, Si–O–Al, and Al–O–Al (T–O–T) of ultimate structure in the High-OH and Low-OH systems at 293 K and 600 K in the Na system and in the K system are shown in Figs. 8 and 9, respectively. The angle distributions are finite-bin histograms; the value at 180° corresponds to the final angular bin containing near-linear T-O-T configurations and should not be interpreted as the probability of exactly 180° angles. In the Na-bearing systems, the T–O–T angle distributions show clear differences between hydroxyl-rich (High-OH) and hydroxyl-poor (Low-OH) conditions. Under High-OH at 293 K (Fig. 8a), the Al–O–Al angles exhibit a strong peak in the 80–90° range, while the Si–O–Si distribution is broad and shifted toward higher angles (roughly 130–180°), indicating a wide range of local connectivities in the aluminosilicate framework. Increasing the temperature to 600 K (Fig. 8c) preserves the same characteristic features, with the low-angle Al–O–Al peak remaining prominent and the Si–O–Si distribution staying broad, although the relative intensities and widths are slightly modified by thermal motion.

When moving from the High-OH to the Low-OH condition (Fig. 8b and 8d), both Si–O–Si and Si–O–Al angle distributions become much more concentrated in the 90–120° range, and their peak intensities increase markedly, indicating a more well-defined and more connected tetrahedral network. The enhanced population of higher-angle Si–O–Si configurations is in line with the increased silicate polymerization inferred from the Q^n analysis. Within each effective alkalinity condition, increasing the temperature from 293 to 600 K leads to moderate changes in peak sharpness and relative intensities, with the Low-OH systems at 600 K showing the narrowest and most pronounced angle distributions. This indicates that effective alkalinity primarily controls the network topology, whereas elevated temperature further promotes structural reorganization toward more well-defined tetrahedral linkages.

In the K systems, the Si–O–Si, Si–O–Al, and Al–O–Al bond-angle distributions are characterized by a dominant peak close to 90–110°, consistent with corner-sharing aluminosilicate tetrahedra. At 293 K, the Low-OH condition exhibits much sharper peaks for Si–O–Al and Al–O–Al. In contrast, the High-OH condition shows broader distributions and a pronounced high-angle contribution for Si–O–Si (extending to about 120–180°), indicating a wider spread of local linkage geometries. Increasing the temperature to 600 K leaves the peak positions essentially unchanged but noticeably sharpens the main peaks, most clearly under High-OH. Overall, moving from the High-OH to the Low-OH condition narrows the tetrahedral-linkage range, while High-OH conditions retain a substantial high-angle Si–O–Si population. The more diffuse K–O coordination environment permits greater rotational freedom of the aluminosilicate tetrahedra and is therefore consistent with the broader T–O–T angle distributions. By contrast, the more localized Na–O interactions spatially confine bond breaking, reconnection, and the associated Q^n redistribution, although effective alkalinity remains the dominant control on overall network polymerization.

3.7. Radius of gyration of nano-clusters as a function of bond-order cutoff

To complement the local Q^n analysis, we further characterize how the aluminosilicate gel connects in the simulation box. For this purpose, nano-clusters are identified as clusters of corner-sharing SiO_4 and AlO_4 tetrahedra, and the connectivity is quantified by the radius of gyration

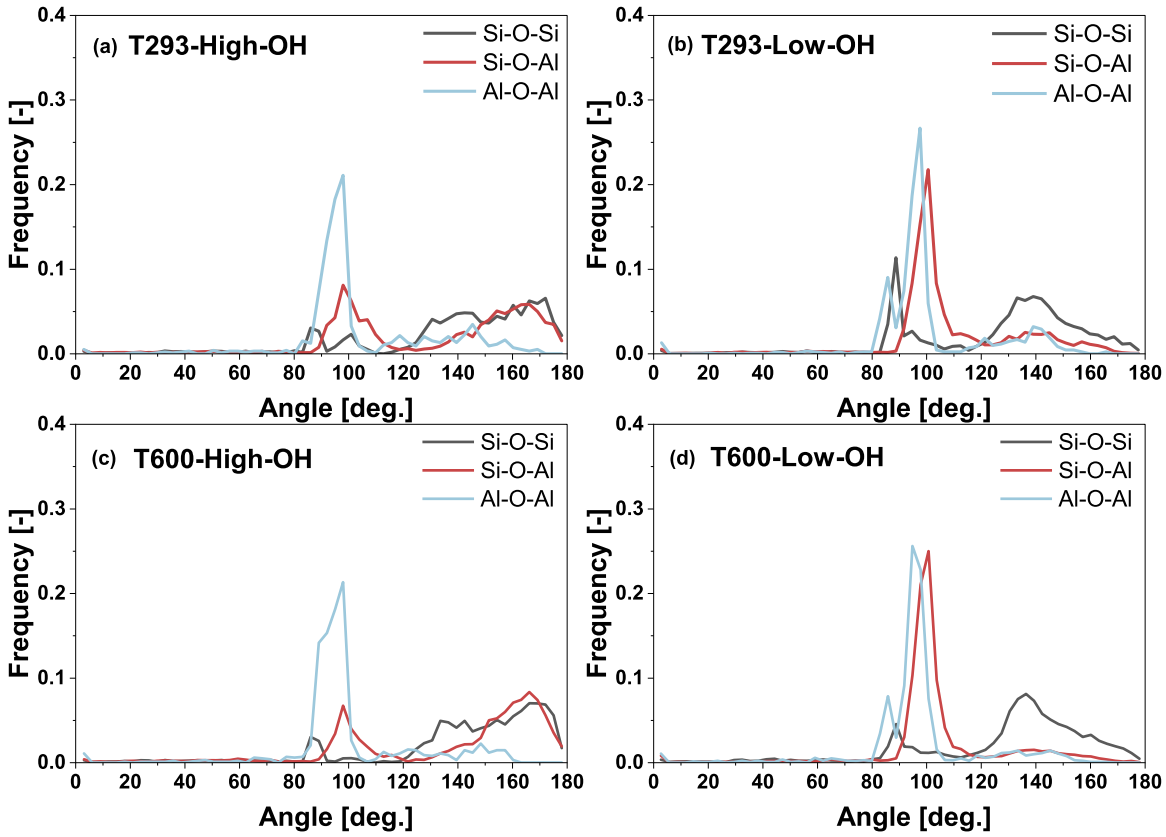


Fig. 8. Bond angle distributions for Si–O-Si, Si–O-Al and Al–O-Al in the High-OH and Low-OH systems at 293 K and 600 K in the Na system.

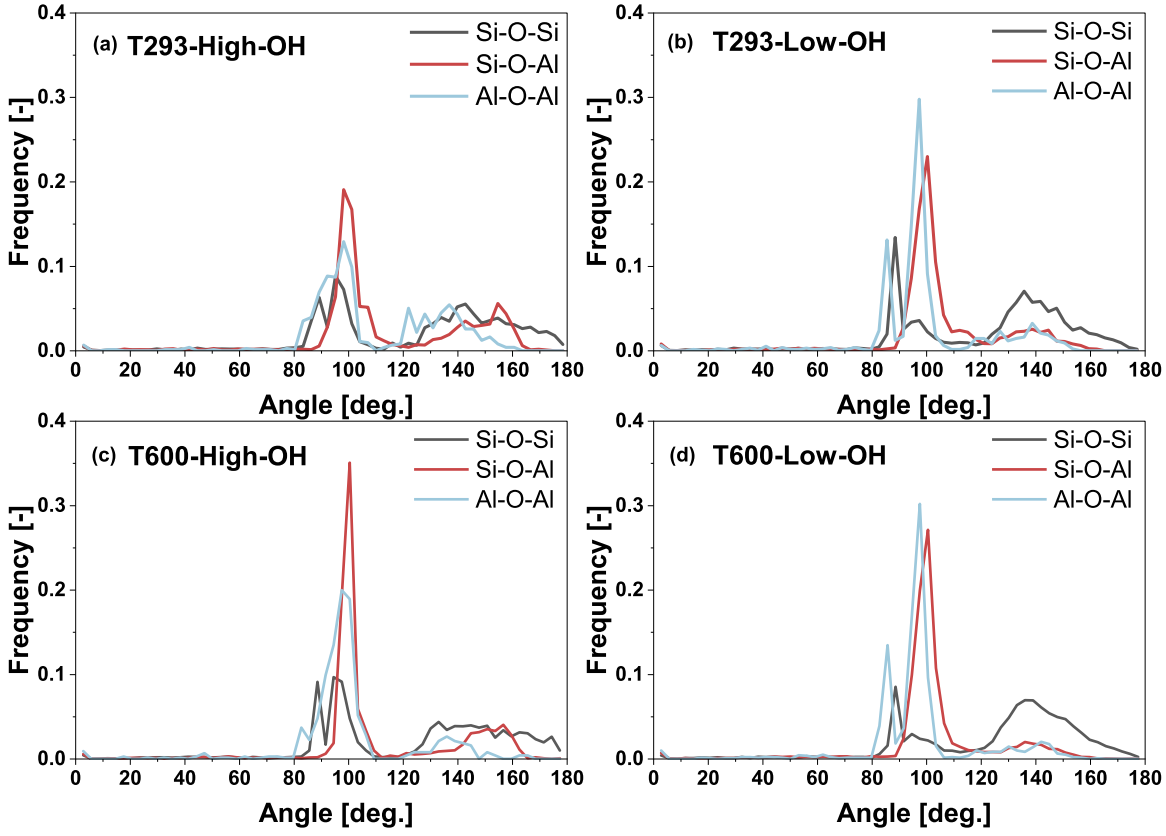


Fig. 9. Bond angle distributions for Si–O-Si, Si–O-Al and Al–O-Al in the High-OH and Low-OH systems at 293 K and 600 K in the K system.

R_g of the largest cluster. The connectivity criterion is controlled by a bond-order cutoff that distinguishes weak, transient interactions from stronger (0.05 to 0.5) and more persistent T–O bonds. By systematically varying this cutoff and monitoring the evolution of R_g, we can separate fragile, weakly bonded aggregates from robust, percolating clusters, thereby directly linking the degree of polymerization to the spatial extent of the gel backbone.

The radius of gyration (R_g) of the largest connected aluminosilicate cluster is shown in Fig. 10 as a function of the bond-order cutoff. Representative cluster morphologies at a fixed cutoff (BO = 0.3) are shown in Fig. 10c for visual reference. In the Na systems (Fig. 10a), R_g is primarily controlled by the effective alkalinity condition and the bond-order criterion. The Low-OH cases yield the largest clusters at weak bond criteria ($R_g \approx 1.5$ nm at low cutoffs) and remain relatively large over intermediate cutoffs, with T600-Low-OH staying around $R_g \approx 1.2$ nm up to BO ≈ 0.3 before decreasing at the strictest cutoffs ($R_g \approx 0.8$ nm at BO = 0.5). The T293-Low-OH curve shows a similar but smaller cluster size (roughly $R_g \approx 0.9$ nm over a broad range of intermediate cutoffs), followed by a decrease at BO = 0.5. Under High-OH, the largest cluster is consistently smaller: T293-High-OH stays near $R_g \approx 0.7$ nm with only weak cutoff dependence, while T600-High-OH drops rapidly from about 1.0 nm at very low cutoff to a plateau around $R_g \approx 0.5$ nm once BO ≥ 0.15. These trends indicate that the Low-OH condition is associated with larger and more persistent connected frameworks that persist even under stricter bond definitions, whereas under High-OH a substantial fraction of connectivity is removed when weak bonds are filtered out (consistent with the snapshots in Fig. 10c at BO = 0.3).

The K systems (Fig. 10b) show the same overall dependence on effective alkalinity conditions and bond-order cutoff. The High-OH curves remain small and only weakly cutoff-dependent (typically $R_g \approx 0.6$ to 0.7 nm). In Low-OH, larger clusters appear when weak bonds are included, especially for T600-Low-OH ($R_g \approx 1.6$ nm at the lowest cutoff), but R_g decreases progressively as the cutoff is tightened, converging to $R_g \approx 0.7$ to 0.8 nm at BO = 0.5. Overall, the bond-order filtering analysis shows that large apparent gel clusters are most robust under Low-OH conditions, while stricter bond criteria systematically reduce the inferred cluster size in all cases.

3.8. $Na_2O(K_2O)$–Al_2O_3–SiO_2 diagram and its implications

The composition of gel-type reaction products within the Na_2O (K_2O)–Al_2O_3–SiO_2 system is highly relevant from both chemical and engineering perspectives and can serve as a criterion for distinguishing N-A-S-H and K-A-S-H clusters from precursors and other reaction products. Previous studies have investigated gel compositions and related phase relations using experimental compositional and microstructural techniques, including BSE imaging coupled with EDX and ICP-OES measurements, as well as thermodynamic assessments [61–66].

The simulations in this work can, in fact, be used to calculate the compositional range within this pseudo-ternary system from a reaction-statistical perspective. To construct the Na_2O(K_2O)–Al_2O_3–SiO_2 ternary composition plots in Fig. 11, we first identified in each simulated configuration the largest connected aluminosilicate gel-like cluster. Then we computed its bulk Na_2O (K_2O), Al_2O_3 and SiO_2 contents by counting atoms whose local environments satisfy the prescribed bond-order criteria (also ranging from 0.05 to 0.5). In addition, the early stage (0 %−10 %), middle stage (45 %–55 %), and late stage (90 %−100 %) of the simulation time were included in the computation. The resulting nano-cluster (size at late stage see Fig. 10) compositions at different bond-order thresholds and reaction stages were projected into ternary space, as summarized in Fig. 11. It should be noted that the 300 ps simulation window is sufficient to obtain quasi-stabilized Q^n distributions and relative compositional trends under the present protocol, but it does not necessarily represent full thermodynamic equilibration of the final gel network, especially for the high-alkalinity systems where later-stage polymerization may proceed more slowly.

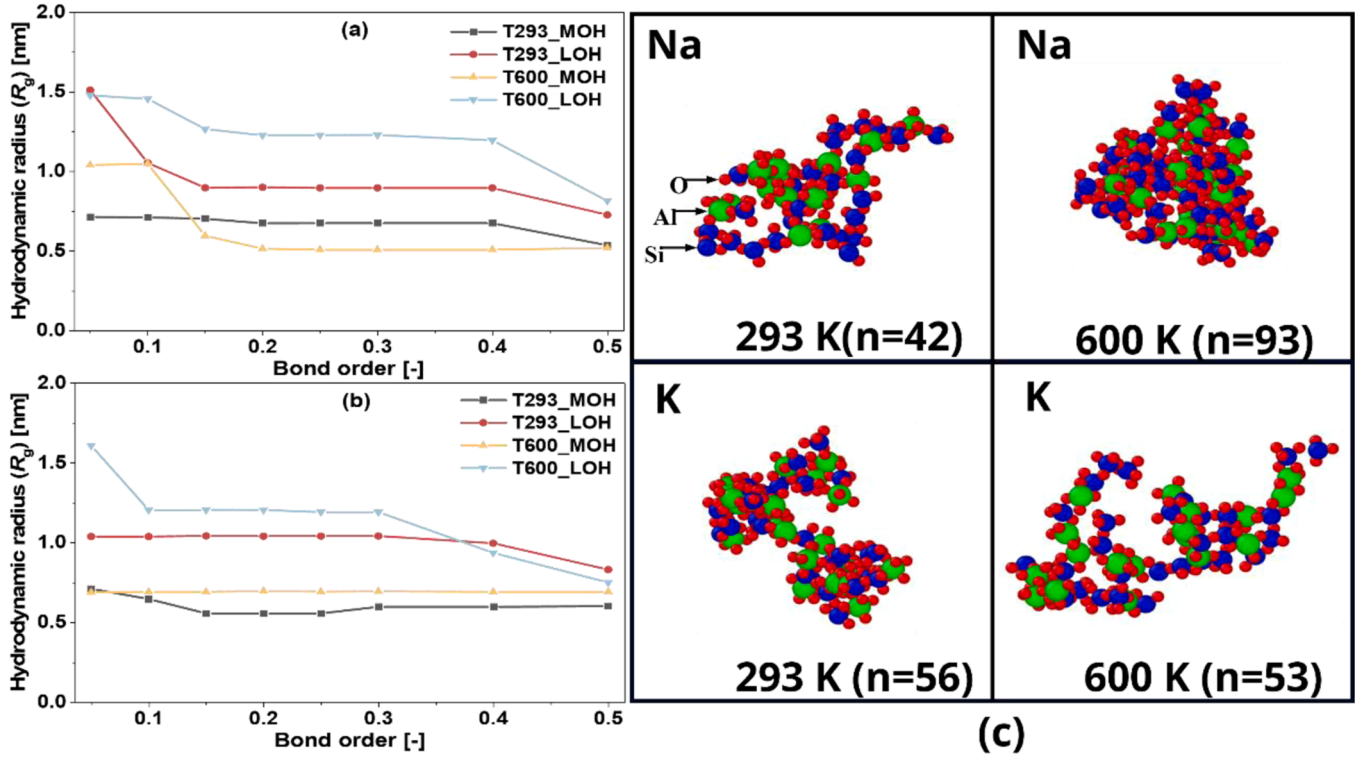


Fig. 10. Radius of gyration (R_g) of the largest connected aluminosilicate cluster as a function of the bond-order cutoff, evaluated using bond-order filtering, for (a) Na and (b) K systems at different temperatures and effective alkalinity conditions. (c) Representative snapshots of the largest cluster for the Low-OH cases, shown for Na (top) and K (bottom) at 293 K and 600 K using a bond-order cutoff of 0.3, illustrating how the apparent cluster size and connectivity decrease as the bond criterion is made more stringent.

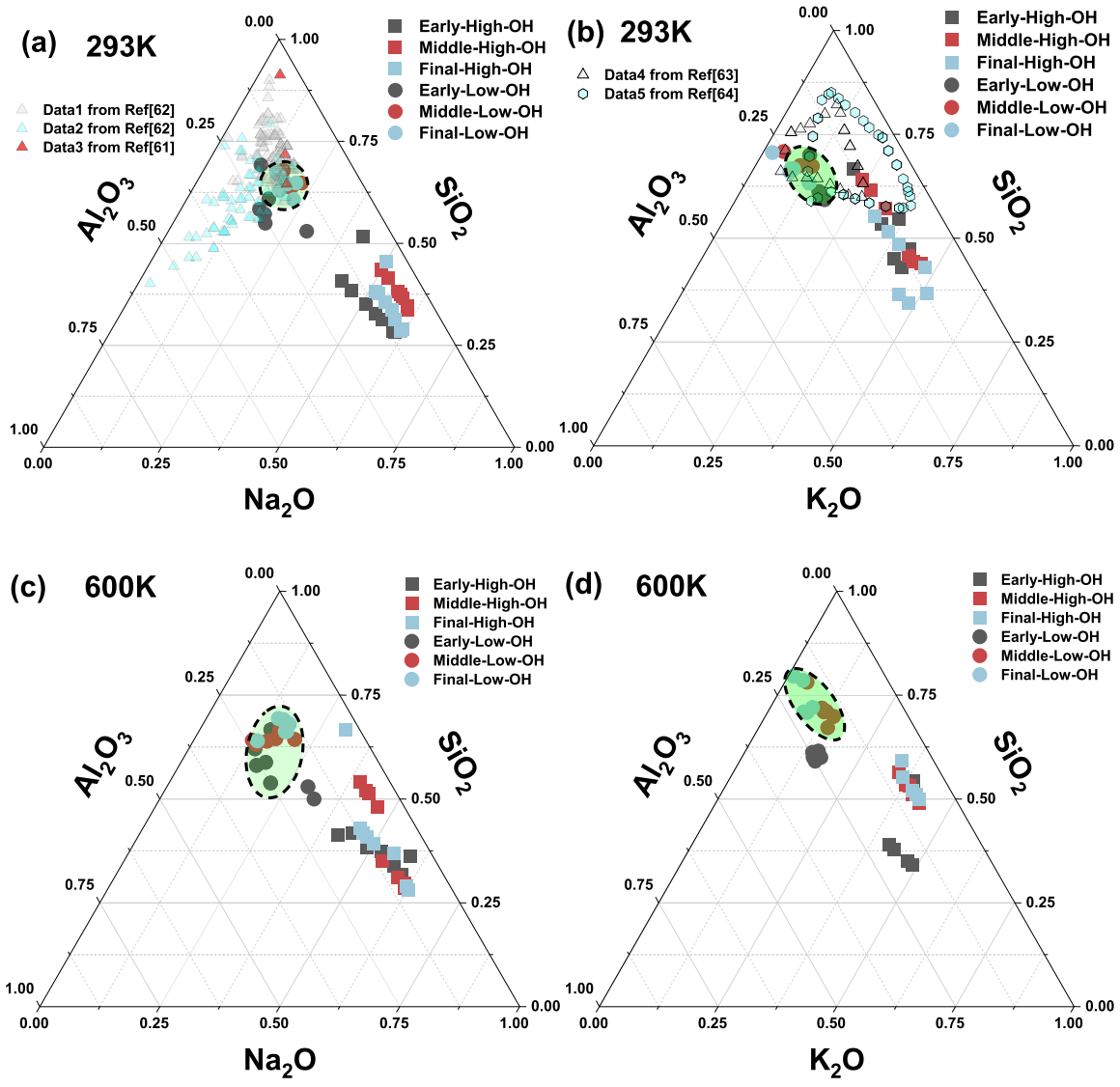


Fig. 11. $Na_2O(K_2O)$–Al_2O_3–SiO_2 ternary diagrams of aluminosilicate cluster compositions extracted from the simulated boxes for Na systems (a, c) and K systems (b, d) at 293 K and 600 K under High-OH and Low-OH conditions at different reaction stages (early, middle, final). For comparison, the data for N-A-S-H taken from Fernández et al. [62] (fly ash mixed with 8 M NaOH and measured by EDX) and Chen et al. [61] (Synthetic N-A-S-H with initial Si/Al 1 to 3), and the data for K aluminosilicate phases ($KAlSi_3O_8$ and $KAlSi_2O_6$) were extracted from Refs [63,64] using thermodynamic CALPHAD calculations for the anhydrous K_2O–Al_2O_3–SiO_2 system.

From the ternary diagrams, it can be seen that under the High-OH effective alkalinity condition, the Na and K contents remain high in both systems, so their compositions occupy regions clearly separated from those of the Low-OH condition samples. Temperature has only a minor influence on the relative proportions of N-A-S-H and K-A-S-H, and the overall distribution pattern is preserved. Under the Low-OH effective alkalinity condition, the compositions of N-A-S-H and K-A-S-H clusters obtained in this work fall within the typical ranges reported in previous studies. Comparison with the fly-ash-based dataset in Ref [62] shows a partial overlap with our simulated N-A-S-H field, although the presence of Ca in fly ash inevitably affects the interpretation of EDX compositions, and this correspondence should be treated with caution. The present Ca-free model is intended to isolate Na or K aluminosilicate network formation. In Ca-bearing alkali-activated systems, C-A-S-H or C-(N, K)-A-S-H formation would introduce Ca-O coordination, modify the charge-balancing environment of AlO_4 tetrahedra, and potentially accelerate precipitation. Therefore, the alkalinity-dependent trends observed here may remain conceptually relevant, but their structural expression is expected to differ in Ca-containing systems.

Notably, the N-A-S-H compositions for the low-alkali systems show excellent agreement with the laboratory-synthesized N-A-S-H reported by Chen et al. [61], and the intersection region highlighted by the dashed circle further confirms the reliability and objectivity of our simulations. In contrast, experimental compositional datasets for K-bearing aluminosilicate gels are scarce; therefore, we use the CALPHAD-derived phase relations of the anhydrous K_2O–Al_2O_3–SiO_2 system [63,64] as a thermodynamic reference for K-aluminosilicate compositions. The CALPHAD-derived reference fields at 293 K (highlighted by the dashed circular/elliptical region) overlap with the present simulation results and remain consistent with the simulated compositional fields at 600 K.

Viewed together with the microscopic descriptors, the $Na_2O(K_2O)$–Al_2O_3–SiO_2 fields identified in Fig. 11 are not only compositional but also structural attractors. The low-alkali N-A-S-H and K-bearing aluminosilicate points that fall within the reported compositional ranges correspond to states with the highest Si and Al Q^n, the lowest BO deprotonation fractions, sharper first-shell Na–O or K–O and T–O peaks in the RDFs, narrow T–O–T angle distributions around 90–120°, and

large, bond-order-resistant clusters with high R_g. In contrast, the high-alkali compositions that plot away from the reported N-A-S-H compositional ranges and the reference K-bearing aluminosilicate domains are associated with more extensive BO deprotonation, broader T–O–T and RDF features, and fragile clusters that rapidly collapse when the bond-order cutoff is increased, confirming that these regions represent more depolymerized and topologically unstable clusters in the $Na_2O(K_2O)$–Al_2O_3–SiO_2 space.

A noteworthy outcome of this work is that it explicitly decouples the role of alkalis in dissolution from their role in subsequent framework formation. In conventional mix-design practice, higher activator dosages are often associated with better performance because they correlate with faster and more extensive dissolution of fly ash or slag at early ages. Our simulations, in contrast, probe a later stage in which a finite pool of SiO_4 and AlO_4 tetrahedra is already in solution and the limiting step is their re-polymerization in a confined volume. In this regime, persistent high alkalinity stabilizes hydroxyl- and alkali-terminated non-bridging oxygens and short aluminosilicate species, thereby slowing the development of an extended N-A-S-H and K-A-S-H backbone. The most polymerized structural signatures in our $Na_2O(K_2O)$–Al_2O_3–SiO_2 diagrams are observed at lower effective alkalinity, where electroneutrality is maintained by a reduced but finite population of charge-balancing Na^+ or K^+. Under the present model conditions, higher residual alkalinity was associated with lower aluminosilicate network connectivity.

4. Conclusions

This study used atomistic simulations to examine how alkali type, effective alkalinity, and temperature affect the structure and connectivity of aluminosilicate clusters formed from dissolved tetrahedral species. The main outcomes are:

(1) Lowering the effective alkalinity (Low-OH condition) promotes polymerization in both Na- and K-bearing systems, shifting Si and especially Al from Q^0–Q^1 toward Q^2–Q^4. Raising the simulation temperature from 293 to 600 K further increases polymerization and network reorganization, particularly under the Low-OH condition. These results indicate that effective alkalinity primarily controls the framework charge environment, whereas higher temperature favors structural rearrangement toward greater connectivity.
(2) Bridging-oxygen deprotonation increases with effective alkalinity and temperature, producing more highly charged frameworks under High-OH conditions, whereas Low-OH systems remain less deprotonated and more polymerized. RDFs and T–O–T angle distributions show that Low-OH conditions yield sharper first-shell T–O and alkali–O correlations and more narrowly focused T–O–T angles around 90–120°, while High-OH conditions exhibit broader and more weakly constrained local environments.
(3) Cluster analysis demonstrates that Low-OH conditions stabilize larger and more persistent connected aluminosilicate clusters, whereas High-OH conditions yield only small or weakly connected aggregates once weak bonds are excluded by bond-order filtering. This indicates that extended cluster connectivity is sustained primarily by strong framework linkages that develop under reduced alkalinity, while High-OH environments are dominated by transient or weakly bonded connections.
(4) The low-alkali compositions fall within reported compositional ranges of N-A-S-H gels and plausible K-aluminosilicate compositional domains, whereas the high-alkali compositions lie outside these regions and correspond to more depolymerized and less topologically stable structures. Under the conditions examined here, higher residual alkalinity is associated with lower aluminosilicate network connectivity.

Future work should relate the structural descriptors identified here to mechanical and transport properties by combining larger-scale simulations with targeted experiments, and extend the present Na or K-only, short-time simulations to Ca-bearing systems, longer time scales, and more complex solution chemistries using advanced sampling or reactive force fields. The $Na_2O(K_2O)$–Al_2O_3–SiO_2 ternary framework developed here also provides a quantitative tool for composition design that can be tested by parametric studies, laboratory synthesis, and in-situ NMR or scattering measurements, in particular for the Si-rich Na-gel and Al-rich K-gel domains.

CRediT authorship contribution statement

Yanliang Ji: Writing – review & editing, Writing – original draft, Visualization, Validation, Software, Resources, Methodology, Investigation, Formal analysis, Data curation, Conceptualization. **Tamino Hirsch:** Writing – review & editing, Writing – original draft, Validation, Methodology, Formal analysis. **Thomas Matschei:** Validation, Supervision, Project administration, Funding acquisition, Formal analysis. **Dietmar Stephan:** Writing – review & editing, Writing – original draft, Supervision, Software, Resources, Project administration, Investigation, Funding acquisition, Formal analysis, Data curation.

Declaration of competing interest

The authors declare that they have no known competing financial interests or personal relationships that could have appeared to influence the work reported in this paper.

Acknowledgements

The authors gratefully acknowledge the German Research Foundation (DFG) Priority program “Net-Zero Concrete” (SPP 2436), project “Thermodynamic Data for Production and Utilization of Net-Zero Binders (DatProBind)” (grant number 542143260). The authors gratefully acknowledge the North-German Supercomputing Alliance (HLRN) and the Resource Allocation Board for providing computing time on the supercomputer Emmy/Grete at NHR-Nord@Göttingen as part of the NHR infrastructure. The calculations for this research were conducted under project nik00113. We further thank Ralf Duda at Technische Universität Berlin for his guidance on accessing and using these HPC resources.

Data availability

The data supporting the findings of this study are available from the corresponding author upon reasonable request.

References

[1] J. Davidovits, Geopolymers, J. Therm. Anal. 37 (1991) 1633–1656, https://doi.org/10.1007/BF01912193.
[2] J.L. Provis, S.A. Bernal, Geopolymers and related alkali-activated materials, Annu. Rev. Mater. Res. 44 (2014) 299–327, https://doi.org/10.1146/annurev-matsci-070813-113515.
[3] W.M. Kriven, C. Leonelli, J.L. Provis, A.R. Boccaccini, C. Attwell, V.S. Ducman, C. Ferone, S. Rossignol, T. Luukkonen, J.S.J. van Deventer, J.V. Emiliano, J. E. Lombardi, Why geopolymers and alkali-activated materials are key components of a sustainable world: a perspective contribution, J. Am. Ceram. Soc. 107 (2024) 5159–5177, https://doi.org/10.1111/jace.19828.
[4] J.L. Provis, J.S.J. van Deventer, Geopolymers, Woodhead Publishing Limited, 2009, https://doi.org/10.1533/9781845696382.
[5] M.S. Aiman, I. Othman, A. Waqar, N. Hamah Sor, H.F. Isleem, H.M. Najm, O. Benjeddou, M.M.S. Sabri, Geopolymers: enhancing environmental safety and sustainability in construction, Civ. Eng. J. 10 (2024) 3350–3369, https://doi.org/10.28991/CEJ-2024-010-10-015.
[6] M.T. Marvila, A.R.G. de Azevedo, L.B. de Oliveira, G. de Castro Xavier, C.M. F. Vieira, Mechanical, physical and durability properties of activated alkali cement based on blast furnace slag as a function of %Na2O, Case Stud. Constr. Mater. 15 (2021) e00723, https://doi.org/10.1016/j.cscm.2021.e00723.
[7] N. Shehata, O.A. Mohamed, E.T. Sayed, M.A. Abdelkareem, A.G. Olabi, Geopolymer concrete as green building materials: recent applications, sustainable

development and circular economy potentials, Sci. Total Environ. 836 (2022) 155577, https://doi.org/10.1016/j.scitotenv.2022.155577.
[8] G.M. Nasab, F. Golestanifard, K.J.D. MacKenzie, The effect of the SiO2/Na2O ratio in the structural modification of metakaolin-based geopolymers studied by XRD, FTIR and MAS-NMR, J. Ceram. Sci. Technol. 5 (2014) 185–191, https://doi.org/10.4416/JCST2014-00007.
[9] P.S. Singh, T. Bastow, M. Trigg, Structural studies of geopolymers by 29Si and 27Al MAS-NMR, J. Mater. Sci. 40 (2005) 3951–3961, https://doi.org/10.1007/s10853-005-1915-x.
[10] P.S. Singh, M. Trigg, I. Burgar, T. Bastow, Geopolymer formation processes at room temperature studied by 29Si and 27Al MAS-NMR, Mater. Sci. Eng., A 396 (2005) 392–402, https://doi.org/10.1016/j.msea.2005.02.002.
[11] P. Duxson, A. Fernández-Jiménez, J.L. Provis, G.C. Lukey, A. Palomo, J.S.J. van Deventer, Geopolymer technology: the current state of the art, J. Mater. Sci. 42 (2007) 2917–2933, https://doi.org/10.1007/s10853-006-0637-z.
[12] P. Duxson, G.C. Lukey, F. Separovic, J.S.J. van Deventer, Effect of Alkali cations on aluminum incorporation in geopolymeric gels, Ind. Eng. Chem. Res. 44 (2005) 832–839, https://doi.org/10.1021/ie0494216.
[13] C. Li, H. Sun, L. Li, A review: the comparison between alkali-activated slag (Si + Ca) and metakaolin (Si + Al) cements, Cem. Concr. Res. 40 (2010) 1341–1349, https://doi.org/10.1016/j.cemconres.2010.03.020.
[14] B. Walkley, X. Ke, O. Hussein, J.L. Provis, Thermodynamic properties of sodium aluminosilicate hydrate (N–A–S–H), Dalton Trans. 50 (2021) 13968–13984, https://doi.org/10.1039/D1DT02202D.
[15] S.H. Hajiabadi, M. Khalifeh, R. van Noort, P.H. Silva Santos Moreira, Review on geopolymers as wellbore sealants: state of the art optimization for CO_2 exposure and perspectives, ACS Omega 8 (2023) 23320–23345, https://doi.org/10.1021/acsomega.3c01777.
[16] H. Wan, L. Yuan, Y. Zhang, Insight into the leaching of sodium alumino-silicate hydrate (N-A-S-H) gel: a molecular dynamics study, Front. Mater. 7 (2020), https://doi.org/10.3389/fmats.2020.00056.
[17] D. Hou, Y. Zhang, T. Yang, J. Zhang, H. Pei, J. Zhang, J. Jiang, T. Li, Molecular structure, dynamics, and mechanical behavior of sodium aluminosilicate hydrate (NASH) gel at elevated temperature: a molecular dynamics study, Phys. Chem. Chem. Phys. 20 (2018) 20695–20711, https://doi.org/10.1039/C8CP03411G.
[18] R. Gupta, A.S. Tomar, D. Mishra, S.K. Sanghi, Multinuclear MAS NMR characterization of fly-ash-based advanced sodium aluminosilicate geopolymer: exploring solid-State reactions, ChemistrySelectChemistrySelect 5 (2020) 4920–4927, https://doi.org/10.1002/slct.202000203.
[19] J.L. Provis, A. Palomo, C. Shi, Advances in understanding alkali-activated materials, Cem. Concr. Res. 78 (2015) 110–125, https://doi.org/10.1016/j.cemconres.2015.04.013.
[20] M. Lahoti, K.K. Wong, K.H. Tan, E.-H. Yang, Effect of alkali cation type on strength endurance of fly ash geopolymers subject to high temperature exposure, Mater. Des. 154 (2018) 8–19, https://doi.org/10.1016/j.matdes.2018.05.023.
[21] Q. Tang, M. Sun, X. Lu, D. Hou, M. Li, P. Wang, Understanding erosion resistance mechanisms of sodium aluminate silicate hydrate in erosion environments: a molecular dynamics study, RSC Adv. 14 (2024) 10397–10408, https://doi.org/10.1039/D4RA00302K.
[22] G. Moutaoukil, S. Alehyen, I. Sobrados, M. Taibi, Microstructural and 29Si and 27Al MAS NMR spectroscopic evaluations of alkali cation and curing effects on class C fly ash-based geopolymer, Chem. Data Collect. 41 (2022) 100898, https://doi.org/10.1016/j.cdc.2022.100898.
[23] Y. Lei, X. Zha, Research on the reaction kinetics of alkali-activated materials, Mag. Concr. Res. 77 (2025) 145–153, https://doi.org/10.1680/jmacr.24.00194.
[24] C. Cui, Y. Dang, C. Luo, L. Wang, H. Peng, Mechanical properties and reaction kinetics of alkali-activated metakaolin, Materials 17 (2024) 367, https://doi.org/10.3390/ma17020367.
[25] L. Valentini, Modeling dissolution–Precipitation kinetics of alkali-activated metakaolin, ACS Omega 3 (2018) 18100–18108, https://doi.org/10.1021/acsomega.8b02380.
[26] Y. Ji, L. Pel, X. Zhang, Z. Sun, Cl- and Na+ ions binding in slag and fly ash cement paste during early hydration as studied by 1H, 35Cl and 23Na NMR, Constr. Build. Mater. 266 (2021) 121606, https://doi.org/10.1016/j.conbuildmat.2020.121606.
[27] Y. Ji, X. Zhang, L. Pel, Z. Sun, NMR investigations on Cl− and Na+ ion binding during the early hydration process of C3S, C3A and cement paste: a combined modelling and experimental study, Compos. B Eng. 283 (2024) 111624, https://doi.org/10.1016/j.compositesb.2024.111624.
[28] Y. Ji, Z. Sun, C. Chen, L. Pel, A. Barakat, Setting characteristics, mechanical properties and microstructure of cement pastes containing accelerators mixed with superabsorbent polymers (SAPs): an NMR study combined with additional methods, Materials 12 (2019) 315, https://doi.org/10.3390/ma12020315.
[29] S.-M. Park, J.-G. Jang, S.-A. Chae, H.-K. Lee, An NMR spectroscopic investigation of aluminosilicate gel in alkali-activated fly ash in a CO2-rich environment, Materials 9 (2016) 308, https://doi.org/10.3390/ma9050308.
[30] M. Criado, A. Fernández-Jiménez, A. Palomo, Alkali activation of fly ash: effect of the SiO2/Na2O ratio, Microporous Mesoporous Mater. 106 (2007) 180–191, https://doi.org/10.1016/j.micromeso.2007.02.055.
[31] Y. Chen, J.S. Dolado, Z. Li, S. Yin, Q. Yu, A. Kostiuchenko, G. Ye, A molecular dynamics study of N–A–S–H gel with various Si/Al ratios, J. Am. Ceram. Soc. 105 (2022) 6462–6474, https://doi.org/10.1111/jace.18597.
[32] M. Hanifa, U. Sharma, P.C. Thapliyal, L.P. Singh, Study on C-A-S-H to N-A-S-H gel conversion in fly ash-based alkali activated aggregates via accelerated carbonation: enhancing performance and inhibiting efflorescence, J. Sustain. Cem. Based. Mater. 14 (2025) 178–197, https://doi.org/10.1080/21650373.2024.2431512.
[33] L. Deng, S. Urata, Y. Takimoto, T. Miyajima, S.H. Hahn, A.C.T. van Duin, J. Du, Structural features of sodium silicate glasses from reactive force field-based molecular dynamics simulations, J. Am. Ceram. Soc. 103 (2020) 1600–1614, https://doi.org/10.1111/jace.16837.
[34] Y. Yu, B. Wang, M. Wang, G. Sant, M. Bauchy, Reactive molecular dynamics simulations of sodium silicate glasses — toward an improved understanding of the structure, Int. J. Appl. Glass. Sci. 8 (2017) 276–284, https://doi.org/10.1111/ijag.12248.
[35] R. Dongol, L. Wang, A.N. Cormack, S.K. Sundaram, Molecular dynamics simulation of sodium aluminosilicate glass structures and glass surface-water reactions using the reactive force field (ReaxFF), Appl. Surf. Sci. 439 (2018) 1103–1110, https://doi.org/10.1016/j.apsusc.2017.12.180.
[36] M. Izadifar, N. Ukrainczyk, E. Koenders, Silicate dissolution mechanism from metakaolinite using density functional theory, Nanomaterials 13 (2023) 1196, https://doi.org/10.3390/nano13071196.
[37] T. Raz, U. Even, R.D. Levine, Fragment size distribution in cluster impact: shattering versus evaporation by a statistical approach, J. Chem. Phys. 103 (1995) 5394–5409, https://doi.org/10.1063/1.470575.
[38] P. Van der Weeën, J.M. Baetens, B. De Baets, Design and parameterization of a stochastic cellular automaton describing a chemical reaction, J. Comput. Chem. 32 (2011) 1952–1961, https://doi.org/10.1002/jcc.21779.
[39] M.R. Sadat, S. Bringuier, A. Asaduzzaman, K. Muralidharan, L. Zhang, A molecular dynamics study of the role of molecular water on the structure and mechanics of amorphous geopolymer binders, J. Chem. Phys. 145 (2016), https://doi.org/10.1063/1.4964301.
[40] M. Zhang, N.A. Deskins, G. Zhang, R.T. Cygan, M. Tao, Modeling the polymerization process for geopolymer synthesis through reactive molecular dynamics simulations, J. Phys. Chem. C 122 (2018) 6760–6773, https://doi.org/10.1021/acs.jpcc.8b00697.
[41] H.C. Edwards, C.R. Trott, D. Sunderland, Kokkos: enabling manycore performance portability through polymorphic memory access patterns, J. Parallel. Distrib. Comput. 74 (2014) 3202–3216, https://doi.org/10.1016/j.jpdc.2014.07.003.
[42] A.P. Thompson, H.M. Aktulga, R. Berger, D.S. Bolintineanu, W.M. Brown, P. S. Crozier, P.J. in 't Veld, A. Kohlmeyer, S.G. Moore, T.D. Nguyen, R. Shan, M. J. Stevens, J. Tranchida, C. Trott, S.J. Plimpton, LAMMPS - a flexible simulation tool for particle-based materials modeling at the atomic, meso, and continuum scales, Comput. Phys. Commun. 271 (2022) 108171, https://doi.org/10.1016/j.cpc.2021.108171.
[43] C. Trott, L. Berger-Vergiat, D. Poliakoff, S. Rajamanickam, D. Lebrun-Grandie, J. Madsen, N. Al Awar, M. Gligoric, G. Shipman, G. Womeldorff, The Kokkos EcoSystem: comprehensive performance portability for high performance computing, Comput. Sci. Eng. 23 (2021) 10–18, https://doi.org/10.1109/MCSE.2021.3098509.
[44] Z. Li, J. Zhang, M. Wang, Structure, reactivity, and mechanical properties of sustainable geopolymer material: a reactive molecular dynamics study, Front. Mater. 7 (2020), https://doi.org/10.3389/fmats.2020.00069.
[45] M. Łach, K. Korniejenko, J. Walter, A. Stefańska, J. Mikuła, Decreasing of leaching and improvement of geopolymer properties by addition of aluminum calcium cements and titanium oxide, Materials 13 (2020) 495, https://doi.org/10.3390/ma13030495.
[46] Y. Zhang, X. Liu, A.C.T. van Duin, X. Lu, E.J. Meijer, Development and validation of a general-purpose ReaxFF reactive force field for earth material modeling, J. Chem. Phys. 160 (2024), https://doi.org/10.1063/5.0194486.
[47] A.C.T. van Duin, S. Dasgupta, F. Lorant, W.A. Goddard, ReaxFF: a reactive force field for hydrocarbons, J. Phys. Chem. A 105 (2001) 9396–9409, https://doi.org/10.1021/jp004368u.
[48] S. Plimpton, Fast parallel algorithms for short-range molecular dynamics, J. Comput. Phys. 117 (1995) 1–19, https://doi.org/10.1006/jcph.1995.1039.
[49] A. Amritkar, D. Tafti, R. Liu, R. Kufrin, B. Chapman, OpenMP parallelism for fluid and fluid-particulate systems, Parallel Comput. 38 (2012) 501–517, https://doi.org/10.1016/j.parco.2012.05.005.
[50] B. Walkley, G.J. Rees, R. San Nicolas, J.S.J. van Deventer, J.V. Hanna, J.L. Provis, New structural model of hydrous sodium aluminosilicate gels and the role of charge-balancing extra-framework Al, J. Phys. Chem. C 122 (2018) 5673–5685, https://doi.org/10.1021/acs.jpcc.8b00259.
[51] P. Duxson, J.L. Provis, G.C. Lukey, F. Separovic, J.S.J. van Deventer, 29Si NMR study of structural ordering in aluminosilicate geopolymer gels, LangmuirLangmuir 21 (2005) 3028–3036, https://doi.org/10.1021/la047336x.
[52] K. Leung, I.M.B. Nielsen, L.J. Criscenti, Elucidating the bimodal acid−base behavior of the water−silica interface from First principles, J. Am. Chem. Soc. 131 (2009) 18358–18365, https://doi.org/10.1021/ja906190t.
[53] L.T. Zhuravlev, The surface chemistry of amorphous silica. Zhuravlev model, Colloids. Surf. A Physicochem. Eng. Asp. 173 (2000) 1–38, https://doi.org/10.1016/S0927-7757(00)00556-2.
[54] M. Sulpizi, M.-P. Gaigeot, M. Sprik, The silica–water interface: how the silanols determine the surface acidity and modulate the water properties, J. Chem. Theory Comput. 8 (2012) 1037–1047, https://doi.org/10.1021/ct2007154.
[55] S. Varma, S.B. Rempe, Coordination numbers of alkali metal ions in aqueous solutions, Biophys. Chem. 124 (2006) 192–199, https://doi.org/10.1016/j.bpc.2006.07.002.
[56] A. Winkler, J. Horbach, W. Kob, K. Binder, Structure and diffusion in amorphous aluminum silicate: a molecular dynamics computer simulation, J. Chem. Phys. 120 (2004) 384–393, https://doi.org/10.1063/1.1630562.
[57] P. Ganster, M. Benoit, W. Kob, J.-M. Delaye, Structural properties of a calcium aluminosilicate glass from molecular-dynamics simulations: a finite size effects

study, J. Chem. Phys. 120 (2004) 10172–10181, https://doi.org/10.1063/1.1724815.
[58] J.F. Stebbins, Anionic speciation in sodium and potassium silicate glasses near the metasilicate ([Na,K]2SiO3) composition: 29Si, 17O, and 23Na MAS NMR, J. Non-Cryst. Solids: X 6 (2020) 100049, https://doi.org/10.1016/j.nocx.2020.100049.
[59] S. Sen, R.E. Youngman, NMR study of Q-speciation and connectivity in K_2O–SiO_2 glasses with high silica content, J. Non. Cryst. Solids 331 (2003) 100–107, https://doi.org/10.1016/j.jnoncrysol.2003.08.071.
[60] M. Carrillo-Tripp, H. Saint-Martin, I. Ortega-Blake, A comparative study of the hydration of Na+ and K+ with refined polarizable model potentials, J. Chem. Phys. 118 (2003) 7062–7073, https://doi.org/10.1063/1.1559673.
[61] Y. Chen, L.M. de Lima, Z. Li, B. Ma, B. Lothenbach, S. Yin, Q. Yu, G. Ye, Synthesis, solubility and thermodynamic properties of N-A-S-H gels with various target Si/Al ratios, Cem. Concr. Res. 180 (2024) 107484, https://doi.org/10.1016/j.cemconres.2024.107484.
[62] A. Fernández-Jiménez, I. Garcia-Lodeiro, O. Maltseva, A. Palomo, Mechanical-chemical activation of coal fly ashes: an effective way for recycling and make cementitious materials, Front. Mater. 6 (2019), https://doi.org/10.3389/fmats.2019.00051.
[63] E. Yazhenskikh, K. Hack, M. Müller, Critical thermodynamic evaluation of oxide systems relevant to fuel ashes and slags, part 5: potassium oxide–alumina–silica, Calphad 35 (2011) 6–19, https://doi.org/10.1016/j.calphad.2010.10.010.
[64] J. Yang, L. Yan, L. Ye, G. Xiao, K. Wang, Y. Liu, L. Zhang, L. Liu, Y. Du, Thermodynamic evaluation and optimization of the K $_2$ O-Al $_2$ O $_3$ -SiO $_2$ system, J. Am. Ceram. Soc. 107 (2024) 8732–8745, https://doi.org/10.1111/jace.20093.
[65] T.A. Aiken, J. Kwasny, W. Sha, Performance of cementless binders produced from industrial waste products in strong acid, Clean. Eng. Technol. 2 (2021) 100035, https://doi.org/10.1016/j.clet.2020.100035.
[66] N. Ranjbar, A. Kashefi, G. Ye, M. Mehrali, Effects of heat and pressure on hot-pressed geopolymer, Constr. Build. Mater. 231 (2020) 117106, https://doi.org/10.1016/j.conbuildmat.2019.117106.